Published in final edited form as:
Nat Neurosci. ; 14(12): 1599–1605. doi:10.1038/nn.2973.

Flexible, Foldable, Actively Multiplexed, High-Density Electrode Array for Mapping Brain Activity *in vivo*

Jonathan Viventi[1,2,⊥], **Dae-Hyeong Kim**[3,⊥], **Leif Vigeland**[4], **Eric S. Frechette**[5], **Justin A. Blanco**[6], **Yun-Soung Kim**[7], **Andrew E. Avrin**[8], **Vineet R. Tiruvadi**[9], **Suk-Won Hwang**[7], **Ann C. Vanleer**[9], **Drausin F. Wulsin**[9], **Kathryn Davis**[5], **Casey E. Gelber**[9], **Larry Palmer**[4], **Jan Van der Spiegel**[8], **Jian Wu**[10], **Jianliang Xiao**[11], **Yonggang Huang**[12], **Diego Contreras**[4], **John A. Rogers**[7], and **Brian Litt**[5,9,*]

[1]Department of Electrical and Computer Engineering, Polytechnic Institute of New York University, Brooklyn, NY 11201 USA

[2]Center for Neural Science, New York University, New York, NY 10003 USA

[3]School of Chemical and Biological Engineering, Seoul National University, Seoul 151-744 Korea

[4]Department of Neuroscience, University of Pennsylvania School of Medicine, 215 Stemmler Hall, Philadelphia, PA 19104 USA

[5]Department of Neurology, Hospital of the University of Pennsylvania, 3 West Gates, 3400 Spruce Street, Philadelphia, PA 19104 USA

[6]Department of Electrical and Computer Engineering, United States Naval Academy, Annapolis, MD 21402 USA

[7]Department of Materials Science and Engineering, Beckman Institute for Advanced Science and Technology and Frederick Seitz Materials Research Laboratory, University of Illinois at Urbana-Champaign, Urbana, Illinois 61801 USA

[8]Department of Electrical and Systems Engineering, University of Pennsylvania, Philadelphia, PA 19104 USA

[9]Department of Bioengineering, University of Pennsylvania, Philadelphia, PA 19104 USA

[10]AML, Department of Engineering Mechanics, Tsinghua Univeristy, Beijing 100084, China

---

[*] To whom correspondence should be addressed. littb@mail.med.upenn.edu; jrogers@uiuc.edu.
[⊥] J. Viventi and D.-H. Kim contributed equally.

AUTHOR CONTRIBUTIONS

J.V., D.-H.K., L.V., A.A., V.T., L.P., J.V.S., D.C., J.A.R. and B.L. designed the experiments. J.V., D.-H.K., L.V., J.A.B., Y.-S.K., S.-W.H., A.C.V., D.F.W., K.D., E.S.F., C.G., R.Y., J.W. and J.X. performed experiments and analysis. J.V., D.-H.K., L.V., J.A.B., E.S.F., Y.H., D.C., J.A.R. and B.L. wrote the paper.

COMPETING FINANCIAL INTERESTS

The authors declare no competing financial interest.

[11]Department of Mechanical Engineering, University of Colorado Boulder, Boulder, CO 80309 USA

[12]Departments of Civil and Environmental Engineering and Mechanical Engineering, Northwestern University, Evanston, IL 60208

Abstract

Arrays of electrodes for recording and stimulating the brain are used throughout clinical medicine and basic neuroscience research, yet are unable to sample large areas of the brain while maintaining high spatial resolution because of the need to individually wire each passive sensor at the electrode-tissue interface. To overcome this constraint, we have developed new devices integrating ultrathin and flexible silicon nanomembrane transistors into the electrode array, enabling new dense arrays of thousands of amplified and multiplexed sensors connected using many fewer wires. We used this system to record novel spatial properties of brain activity *in vivo*, including sleep spindles, single-trial visual evoked responses, and electrographic seizures. Our electrode array allowed us to discover that seizures may manifest as recurrent spiral waves which propagate in the neocortex. The developments reported here herald a new generation of diagnostic and therapeutic brain-machine interface (BMI) devices.

Keywords

Multielectrode array; electrode array; flexible electronics; multiplexed electrode; cortical surface electrode; foldable electrode; ECoG; μECoG; brain machine interface; high temporal resolution; high spatial resolution; spindle; visual neuroscience; spiral wave; epilepsy; seizure; epileptiform spike; interhemispheric fissure; silicon nanoribbon

The utility of high-resolution neural recordings from the cortical surface for basic research and clinical medicine has been shown for a wide range of applications. Spatial spectral analysis of electrocorticograms (ECoG) from the superior temporal gyrus and motor cortex demonstrate that electrode spacing should be 1.25 mm or closer in humans to sufficiently capture the rich spatial information available[1]. Motor control signals[2] and spoken words[3] can be decoded with substantially improved performance utilizing electrodes spaced 1 mm apart or less. In occipital cortex, arrays with 500 μm spacing have demonstrated micro-field evoked potentials that can distinguish ocular dominance columns[4]. The spatial scale for some pathologic signals is also submillimeter, based on observations of microseizures, microdischarges and high frequency oscillations in epileptic brain[5,6].

Yet the subdural electrodes in use clinically, for example, in the diagnosis and treatment of epilepsy, are much larger (~3 mm diameter) and have large interspacing (~10mm) because of the clinical need to record from large areas of the brain surface (80 mm × 80 mm) in order to accurately localize seizure generating brain regions. Large area electrode arrays with high spatial resolution are also needed in BMI applications to account for variability in the location of brain functions, which can vary by ~5mm across subjects[7–10]. High-resolution interface over a large area has previously been impossible due to the infeasibility of connecting thousands of wires in the small intracranial space.

Much of the existing research in electrode technology has focused on penetrating electrode arrays, such as the Utah array[11], which can provide a high-resolution interface to a small area of cortex and enable high-performance neuromotor prostheses[12]. However, arrays of penetrating microelectrodes may only function 6–12 months[13] before the signal quality on most electrodes is substantially diminished. These devices can also cause hemorrhage and inflammatory tissue responses from the immediate insertion[14,15] and over long periods of time, possibly due to the inability of the rigid penetrating electrodes to flex and move as the brain pulses, swells and contracts[16].

Highly flexible arrays of subdural electrodes have unique advantages over penetrating microelectrode arrays in that they are able to maintain signal quality over extended periods of time with minimized irritation and injury to brain tissues[17–20]. Further, the micro-electrocorticographic (μECoG) signal recorded from flexible arrays of non-penetrating electrodes with high-resolution can provide comparable information content to the spiking activity recorded by penetrating microelectrodes in some applications, such as BMI[21–25].

RESULTS

Electrode array fabrication and testing

To enable high-resolution interface with large areas of the brain, we developed an array of flexible, non-penetrating electrodes using novel flexible silicon electronics technology. The array was composed of 720 silicon nanomembrane transistors (Fig. 1a). The active matrix circuit design contained two transistors per unit-cell (Fig. 1b, left frame). The buffer transistor connected to the electrode provided buffering of the biological signals, while the multiplexing transistor allowed all of the electrodes in the same column to share a single output wire. Flexible transistors were fabricated using high-quality single-crystal silicon, yielding a mobility of ~350 cm^2/Vs and an on/off ratio $>10^3$, calculated from the slopes of the transfer curves and the ratio of maximum and minimum current outputs (Fig. 1b, center and right frame) using standard field-effect transistor models[26]. This capability enabled high speed multiplexing (<5 μs), sampling rates > 10 kS/s per electrode[27] and very low multiplexer crosstalk (< −65 dB).

Active electrode arrays were fabricated using a multi-layer process, schematically illustrated in the exploded view in Fig. 1c. Doped silicon nano-ribbons (~260nm) were located in the first layer through the use of transfer printing technology. Subsequent horizontal and vertical metal interconnect layers were insulated using layers of polyimide (PI, ~1.2μm, Sigma Aldrich, USA). Additional polymeric encapsulation layers (PI and epoxy, ~1.2μm and ~4μm) with an offset vertical interconnect access (VIA) structure (Fig. 1c, right panels) prevented electrical leakage currents when the device was immersed in highly conductive bio-fluids. As a final step, platinum (Pt, ~50nm) was evaporated and deposited onto the surface electrodes to reduce their impedance (~20 kOhm at 1 kHz). Detailed fabrication procedures, corresponding microscope images and a cross-sectional schematic can be found in the Online Methods section and in Supplementary Figure 1 online.

Conventional electrode technology is technically limited in its ability to record from inside of sulci. However, implanting even a few electrodes in sulci such as the central sulcus, has shown that the signals obtained carry more information for BMI applications than signals recorded from the traditional gyral surface[28]. Electrical recording from inside sulci may also be important for clinical applications, as studies of brain pathology have demonstrated that focal cortical dysplasias are preferentially located at the bottom of sulci[29]. Some devices have attempted to address this by exposing a small number of passive electrodes on both surfaces of the device[30,31], but only achieved limited spatial sampling.

The extreme flexibility of our device allowed it to be folded around ~700 μm thick silicone rubber, forming a unique, high-resolution, double-sided recording device that allowed access to rarely explored cortical areas, such as the interior of sulci or the medial aspects of the cerebral hemispheres (Fig. 1d). To minimize induced strain in the silicon, silicon dioxide and metal interconnection layers during folding, we reduced the overall array thickness from 76 μm[27] to 25 μm, resulting in a nearly 10-fold reduction in bending stiffness. This was accomplished by reducing the PI substrate thickness from 25 μm (Fig. 1e, blue trace) to 12.5 μm (Fig. 1e, red trace), and by reducing the epoxy encapsulation thickness from 20 μm to 8 μm (Fig. 1e, arrows). The induced strain in each layer during folding was estimated via analytical modeling (Fig. 1f) and was maintained well below the mechanical fracture strain of each inorganic material (~1% for Si and SiO_2[32]).

In vivo experiments

We used our flexible electrode device to map neural activity at high resolution, on the surface of visual cortex of 10 cats *in vivo* (Fig. 2a). An initial craniotomy and durotomy exposed a 2 × 3 cm region of cortex. Eyes were focused on a monitor that subtended 28° × 22° of space. The electrode arrays were either placed on the brain (Fig. 2a) or inserted into the interhemispheric fissure, as shown in the inset of Fig. 2a and Fig. 2b, right frame. Given the high flexibility of the electrode array, it could be placed in between the two hemispheres of the brain without causing damage to tissue. In this configuration, the recording surface is facing the left hemisphere. Alternately, the folded electrode array can be inserted in the same location as the flat electrode array (Fig. 2b, left frame), simultaneously recording from both hemispheres, with the right hemisphere filtered through the dura.

Sleep spindles

We recorded spontaneous spindles during barbiturate anaesthesia in the μECoG signal. Spindle oscillations consisted of waves repeating at 5–7 Hz, lasting 1–2 seconds and repeating every 6–10 seconds. Due to the large number of channels on the electrode array, and the large number of spindles recorded, data from a representative channel is shown for a typical spindle (Fig. 3a). The signal amplitude of ~1.2 mV agreed with earlier published reports[33]. The unfiltered noise level of 30 μV RMS was greatly improved from our previous report[27]. Individual waves within spindle oscillations were identified by a detector triggered on a threshold of two standard deviations above or below the mean. For four of these waves, the root-mean-square (RMS) value of the zero-meaned signal in the 30 ms window before and after the peak is plotted on the array map (Fig. 3b, I–IV, left column). For each channel in the array with > 50% of the maximum RMS value, the time to the peak of the wave was plotted (Fig. 3b, I–IV, right column). We observed individual spindle waves to be spatially confined to a small region of brain (< 5mm × 5mm) and did not move. Spindle waves were highly synchronous, peaking within a few milliseconds in all of the channels involved.

Visual evoked responses

Visual stimuli consisting of full-field drifting gratings were presented for 504 ms at 2 Hz with a spatial frequency of 0.5 cycles per degree. Single-trial visual evoked potentials[34] were visible on many channels of the electrode array. A small subset of these potentials were shown, without averaging, to illustrate the quality of the electrode array recordings (see Supplementary Fig. 2 online).

A second visual stimulus consisted of flashing white boxes at pseudorandom locations within an 8 by 8 grid were presented in order to measure the retinotopic organization of the recorded cortical area. The duration of each flash was 200 ms, followed by a 64 ms blank time. Stimuli were presented 15 times at each location, for a total of 960 stimulus presentations. Responses from the 15 trials were averaged. The response strength for the 64 different stimulus locations was determined for each of the 360 electrode array channels by calculating the RMS value of the zero-meaned signal within the 40 ms to 160 ms window after presentation of the visual stimulus, to capture the majority of the visual evoked potential[34]. Response strengths are plotted in Figure 4a as 64 color maps, each showing the response of the entire 360 channel electrode array. Color maps are arranged in the same physical layout as the stimuli were presented in the visual field, i.e. the image map in the upper left hand corner of the figure represents the neural response recorded from all 360 channels to a flashing box presented in the upper left hand corner of the monitor. The color scale is constant over all 64 image maps and is saturated at the 1st and 99th percentile of recorded response strength, respectively, to improve the visual display. The responses indicate that distinct regions of the brain responded to distinct areas of the visual field, as expected. The electrode color map data is oriented such that the bottom left-hand corner of the electrode array was approximately located over Brodmann area 18, the bottom right-hand corner over area 17, the middle region over areas 18 and 19, the upper right-hand corner over area 21 and upper left-hand corner over area 7 (inset, Fig. 4b).

For each channel in the array with a response > 50% of the peak RMS value (as calculated above), the delay to the peak of the evoked response was determined (Fig. 4b). Channels below threshold are shown as white. A few general observations are visible in the data. Stimuli presented in the lower and left areas of the screen appear to activate small areas of the lower left-hand corner of the electrode array and these responses occurred earliest, consistent with early visual cortical areas[35]. Stimuli presented in middle to upper-middle areas of the visual field appear to elicit responses in large areas of the upper middle areas of the electrode array and these activations occurred later, consistent with visual association cortex. The upper two rows of the screen appeared to be outside of the visual field covered by the array, possibly due to electrode placement not covering the *area striata* activated during stimulation at the upper portion of the visual field.

As a more rigorous test of the ability of the electrode array to resolve the visual field, the evoked response data was used to train a deep belief net (DBN) classifier[36,37]. A training set was generated by randomly selecting 10 out of the 15 trials, averaging the evoked responses and repeating this process 100 times for each of the 64 screen locations to yield 6400 total samples. The evoked response feature vectors were calculated as in Figure 4a and 4b, and concatenated, giving 720 feature dimensions in each of the 6400 samples. The trained deep belief net was tested on a separate dataset of 10 trials, averaged together, from the same animal and recording day. The prediction performance is illustrated as image map of the visual field in Figure 4c. 23 of the 64 screen locations (36%) were predicted exactly correct (black boxes), significantly better than chance (1.6%). 42 of 64 (66%) screen locations were predicted correctly within 1 neighboring square (greyboxes, distance $\leq \sqrt{2}$, chance level 11.8%).

These results validate the capability of the electrode array to resolve visual evoked responses. Increasing prediction accuracy through improved decoding algorithms and optimization of the placement of visual stimuli are the subject of ongoing research in our laboratory. The capability of these electrode arrays to decode natural movies is also being investigated.

Electrographic Seizures

As a third demonstration of this new technology, seizures were induced in the feline model using local administration of picrotoxin. The drug was placed directly on the brain, adjacent to the electrode array on the frontal-medial corner. In one of the animal experiments, the electrode array recorded four spontaneous electrographic seizures and hundreds of interictal spikes over ~1 hr. The μECoG signal from a single channel of the electrode array during a short electrographic seizure (Fig. 5a) demonstrated large amplitude (6.6 mV), low noise (45 μV RMS) and high signal-to-noise ratio (SNR, 34 dB).

The array recorded spatial patterns never previously observed during seizures (Movie M1). At the ictal onset, there was a plane wave (I) coming from the upper left which encountered a phase anisotropy, bent to the right, and anticipated the subsequent clockwise spiral (wave II). This spiral pattern (wave II) rotated for 3 cycles. A second incoming plane wave (III) changed the direction of rotation of the spiral. The ensuing counterclockwise spiral (wave IV) rotated for 19 cycles and was terminated by a plane wave (V) coming from the right.

Based upon these early observations, it is possible that neocortical seizures may be initiated by interictal spikes diverted asymmetrically around regional anisotropies, resulting in sustained reentrant loops. Seizures may be terminated by mutual annihilation of a rotating spiral with a traveling wave, which has implications for electrical stimulation to disrupt seizures[38]. Analogous anisotropies and colliding waves have been observed in the genesis and termination of cardiac arrhythmias[39].

Band-pass filtering the spiral wave data to investigate only the primary frequency component (as in previous analysis[40–42]) yielded delay plots that are consistent with spiral waves. The primary frequency of the counter-clockwise spiral during the seizure was 6 Hz (see Supplementary Fig. 3 online). Spiral wave data was band-pass filtered from 4 to 8 Hz using a 6th order butterworth band-pass filter in the forward and reverse directions, resulting in zero-phase distortion digital filtering (and effectively doubling the order of the filter to a 12th order filter). The relative delay for each electrode was calculated by first upsampling by a factor of 12 and then taking the index of the maximum cross-covariance between each channel and the average of all 360 channels. The resulting delay image map (Fig. 5c) showed a singularity as if forming a counterclockwise rotating pinwheel. Clockwise motion was also demonstrated by the delay plot (Fig. 5d) albeit with a less clear singularity.

In addition to the spatiotemporal patterns analyzed above, the large SNR of the electrode array allowed us to analyze the pattern of single ictal and interictal spikes. Stereotyped, repetitive spatiotemporal patterns of single spikes were frequently observed throughout the dataset. We developed a clustering algorithm to test whether the spatiotemporal patterns of single spikes could be classified consistently. First a standard, threshold-based spike detector was run on the average of all 360 channels to provide event detections. Other methods that leverage signal detection in individual channels may allow better resolution of more localized spikes. The threshold was set at −500 μV with a refractory period of 160 ms, yielding a mean spike amplitude and standard deviation of 2.2 mV and 0.95 mV respectively. The noise amplitude of the averaged signal from all 360 channels was 39 μV or 14 μV RMS. Data from all 360 electrodes in the window 60 ms before and 100 ms after the threshold crossing were upsampled by a factor of 12 and cross-correlated with the average of all 360 channels. The relative delay of the spike on each channel was calculated using the index of the maximum cross-covariance value. Upsampling allowed the relative delays to be computed with subsample time accuracy. In addition, the magnitude of the spike on each channel was calculated using the RMS value of the zero-meaned signal within the same window. The 360-element delay and RMS vectors representing each spike were normalized by dividing by their maximum respective values and concatenated. Using these two features, relative delay and RMS, the speed and direction of the wavefront, as well as its amplitude, could be encoded.

To lessen the computational burden before clustering, principal components analysis (PCA) was used to reduce the dimensionality of the spike data from 720 to 81 – a number of coefficients that accounted for 99% of the data variance. Finally, k-medoids clustering[43] was carried out on 877 detected spikes. The potential number of clusters, k, ranged from 1 (i.e. no clustering) to 30 and the gap statistic[44] was then used to determine the optimal number of clusters[45]. 21 clusters were returned. Delay maps for all of the spikes in each cluster indicated a strong similarity within clusters (see Supplementary Figs. 4 to 14 online).

Example relative delay image maps for six different clusters are shown to illustrate their differences (Fig. 5e, left frames). The events in the six clusters shown were found both ictally and interictally. The representation of each event on a standard clinical electrode, based on the average signal, is plotted as a red trace (Fig. 5e, right). They illustrated that vastly different micro-scale spatial patterns can be indistinguishable on a macro-scale, again strongly motivating recordings from brain at high spatial resolution.

5 of the 21 clusters appeared to occur only during seizures. One example each from two of these clusters is shown (Fig. 5f). These results suggested that μECoG can differentiate ictal from interictal patterns that would show up as nearly identical spikes at the resolution of clinical EEG.

DISCUSSION

The electrode arrays in use today can either sample broad regions of the brain (~80mm × ~80mm) at low spatial resolution (~10mm spacing), or small regions of brain (~4mm × ~4mm) at high spatial resolution (~400μm spacing)[11], with both requiring N wires for N electrodes. Here we have shown a 360-channel active electrode array capable of sampling a 5-fold larger region of brain (10mm × 9mm) than prior work[11], with high spatial resolution (500μm spacing) and high temporal resolution (>10kS/s) while reducing the number of wires 9-fold. This technology offers spatial resolution approaching that of voltage sensitive dyes, with greatly improved temporal resolution and signal to noise ratio, with the ability to record from non-planar and non-optically accessible areas and in a potentially fully implantable, non-toxic, clinical-scale system. This technology can be rapidly scaled to clinical sizes (~80mm × ~80mm) with 25,600 channels, while maintaining high temporal resolution (>1.2kS/s), enabling elucidation of micro-scale brain dynamics in human normal brain activity and disease.

Spiral activity has been described by mathematical models of 2-dimensional excitable media[46] and has been documented in brain and heart[39–42] but until now a tool did not exist to record exhaustive spatiotemporal patterns of brain activity in a large mammalian brain, as we demonstrate here. Our results suggested that spiral waves are present during seizures, though the seizures produced in this case were induced by acute disinhibition and may not accurately represent activity characterizing spontaneous seizures in chronic epilepsy. Perhaps more importantly, our technology offers a method to record this kind of activity chronically, in awake, behaving animals and humans with unprecedented detail.

The significance of high density, active array technology is evident in the neural dynamics which emerge at a spatial scale 400 times finer than used clinically. This technology demonstrated complex spatial patterns, such as spiral waves, clustering of spatiotemporal patterns, and heterogeneity and anisotropy of sleep oscillations, all of which occurred within the space occupied by one current clinical ECoG electrode. Whereas coarse spatial undersampling prevents current technology from resolving the micro-scale spatial patterns that occur in the brain, the high resolution of this active array technology enabled us to distinguish intrinsic from pathologic signals efficiently, even within the same frequency bands.

Our observations suggested that spindles are spatially punctate, stationary, and temporally coherent, whereas epileptiform activity in this model propagates as planar and spiral waves. Further research is needed to fully characterize these preliminary results and their significance. Prior investigations using voltage-sensitive dyes have found spiral waves in rodents during EEG epochs dominated by sleep-like delta frequencies[42], in contrast, we demonstrate activity which was spatially inhomogeneous and did not spiral, yet was present during delta-dominant states, and which appeared as sleep spindles electrographically. While optical imaging has demonstrated spatial patterns such as planar waves and spirals in disinhibited rat cortex[41], high-density, active array technology enabled us to show that these spiral dynamics in disinhibited cat cortex are electrographic seizures at the clinical scale.

Ultimately, the question of clinical relevance is whether there are spiral waves in human cortex, yet voltage sensitive dye recordings are infeasible for use in humans due to the requirement that the brain be optically exposed and subjected to toxic dyes. Our results suggested that technology incorporating flexible, high-density, active arrays of electrodes can provide equal or superior recordings in a fully implantable system. If spiral waves are demonstrated in human cortex, the clinical implications are profound. Seizure control may be analogous to the control of cardiac arrhythmias, which are also known to manifest as reentrant spiral waves of excitation[39]. Further, as learning tasks increase spindle activity[47], which may be due to consolidation and integration of memories[48], understanding the fine structure of spindles has implications for learning and memory efficiency, as well as thalamocortical networks involved in sleep and primary generalized epilepsy.

Finally, flexible devices such as those shown here hold the promise to enable neuroprosthetic devices that have been limited until now by the lack of resolution of the brain-machine interface and by the irregular topography of the brain. Utilizing the extreme flexibility of active electrode arrays, devices can be folded and implanted into currently inaccessible brain regions, such as sulci and fissures, that can be simultaneously recorded and stimulated, along with surface regions to enable devices to facilitate movement, sensation, vision, hearing and cognition. These devices can also be powered remotely through wireless power transmission techniques[49].

Our work also has implications for treating disease. Disorders such as epilepsy, dementia, affective disorders, movement disorders and schizophrenia are all conditions that affect dispersed brain networks, rather than a single locus of brain function. Investigations of major depression, parkinsonism, and chronic pain with magnetoencephalography have identified “thalamocortical dysrhythmia,” but increases of spatial and temporal resolution as with the recording method presented here would allow a more detailed characterization of these diseased networks[50]. Only with new approaches that can resolve micro-scale activity over large areas of cortex will we be able to begin to understand how the brain functions in both disease and health, and to develop better diagnostic and therapeutic options for those affected.

METHODS

Methods and any associated references are available in the online version of the paper at http://www.nature.com/natureneuroscience/.

Note: Supplementary information is available on the Nature Neuroscience website.

Supplementary Material

Refer to Web version on PubMed Central for supplementary material.

Acknowledgments

This material is based upon work supported by the National Science Foundation under grant DMI-0328162 and the U.S. Department of Energy, Division of Materials Sciences under Award No. DE-FG02-07ER46471, through the Materials Research Laboratory and Center for Microanalysis of Materials (DE-FG02-07ER46453) at the University of Illinois at Urbana-Champaign. J.A.R. acknowledges a National Security Science and Engineering Faculty Fellowship. Work at the University of Pennsylvania is supported by the National Institutes of Health Grants (NINDS RO1-NS041811, NINDS R01 NS 48598) and the Dr. Michel and Mrs. Anna Mirowski Discovery Fund for Epilepsy Research. J.V. was supported by the National Institutes of Health under Ruth L. Kirschstein National Research Service Award 2T32HL007954 from the NIH-NHLBI.

References

1. Freeman W. Spatial spectral analysis of human electrocorticograms including the alpha and gamma bands. Journal of Neuroscience Methods. 2000; 95:111–121. [PubMed: 10752481]
2. Kellis SS, House PA, Thomson KE, Brown R, Greger B. Human neocortical electrical activity recorded on nonpenetrating microwire arrays: applicability for neuroprostheses. Neurosurgical focus. 2009; 27:E9. [PubMed: 19569897]
3. Kellis S, et al. Decoding spoken words using local field potentials recorded from the cortical surface. Journal of neural engineering. 2010; 7:056007. [PubMed: 20811093]
4. Kitzmiller JP, et al. Micro-field evoked potentials recorded from the porcine sub-dural cortical surface utilizing a microelectrode array. Journal of neuroscience methods. 2007; 162:155–61. [PubMed: 17298849]
5. Schevon CA, et al. Microphysiology of epileptiform activity in human neocortex. Journal of clinical neurophysiology: official publication of the American Electroencephalographic Society. 2008; 25:321–30. [PubMed: 18997628]
6. Stead M, et al. Microseizures and the spatiotemporal scales of human partial epilepsy. Brain: a journal of neurology. 2010; 133:2789–97. [PubMed: 20685804]
7. Amunts K, Malikovic A, Mohlberg H, Schormann T, Zilles K. Brodmann's areas 17 and 18 brought into stereotaxic space-where and how variable. Neuro Image. 2000; 11:66–84. [PubMed: 10686118]
8. Branco DM, et al. Functional variability of the human cortical motor map: electrical stimulation findings in perirolandic epilepsy surgery. Journal of clinical neurophysiology: official publication of the American Electroencephalographic Society. 2003; 20:17–25. [PubMed: 12684554]
9. Fox PT, et al. Location-probability profiles for the mouth region of human primary motor-sensory cortex: model and validation. Neuro Image. 2001; 13:196–209. [PubMed: 11133322]
10. Van Essen DC, Newsome WT, Maunsell JH. The visual field representation in striate cortex of the macaque monkey: asymmetries, anisotropies, and individual variability. Vision research. 1984; 24:429–48. [PubMed: 6740964]
11. Campbell PK, Jones KE, Huber RJ, Horch KW, Normann R. a A silicon-based, three-dimensional neural interface: manufacturing processes for an intracortical electrode array. IEEE transactions on bio-medical engineering. 1991; 38:758–68. [PubMed: 1937509]
12. Hochberg LR, et al. Neuronal ensemble control of prosthetic devices by a human with tetraplegia. Nature. 2006; 442:164–71. [PubMed: 16838014]
13. Ryu SI, Shenoy KV. Human cortical prostheses: lost in translation? Neurosurgical focus. 2009; 27:E5. [PubMed: 19569893]
14. Polikov VS, Tresco PA, Reichert WM. Response of brain tissue to chronically implanted neural electrodes. Journal of neuroscience methods. 2005; 148:1–18. [PubMed: 16198003]
15. Schmidt S, Horch K, Normann R. Biocompatibility of silicon-based electrode arrays implanted in feline cortical tissue. Journal of biomedical materials research. 1993; 27:1393–9. [PubMed: 8263001]
16. Griffith RW, Humphrey DR. Long-term gliosis around chronically implanted platinum electrodes in the Rhesus macaque motor cortex. Neuroscience letters. 2006; 406:81–6. [PubMed: 16905255]
17. Margalit E. Visual and electrical evoked response recorded from subdural electrodes implanted above the visual cortex in normal dogs under two methods of anesthesia. Journal of Neuroscience Methods. 2003; 123:129–137. [PubMed: 12606062]
18. Chao ZC, Nagasaka Y, Fujii N. Long-term asynchronous decoding of arm motion using electrocorticographic signals in monkeys. Frontiers in neuroengineering. 2010; 3:3. [PubMed: 20407639]

19. Yeager JD, Phillips DJ, Rector DM, Bahr DF. Characterization of flexible ECoG electrode arrays for chronic recording in awake rats. Journal of neuroscience methods. 2008; 173:279–85. [PubMed: 18640155]
20. Yu Z, et al. Monitoring hippocampus electrical activity in vitro on an elastically deformable microelectrode array. Journal of neurotrauma. 2009; 26:1135–45. [PubMed: 19594385]
21. Andersen RA, Musallam S, Pesaran B. Selecting the signals for a brain-machine interface. Current opinion in neurobiology. 2004; 14:720–6. [PubMed: 15582374]
22. Mehring C, et al. Inference of hand movements from local field potentials in monkey motor cortex. Nature neuroscience. 2003; 6:1253–4. [PubMed: 14634657]
23. Ball T, et al. Towards an implantable brain-machine interface based on epicortical field potentials. Biomed Tech (Berlin). 2004; 38:756–759.
24. Wilson JA, Felton EA, Garell PC, Schalk G, Williams JC. ECoG factors underlying multimodal control of a brain-computer interface. IEEE transactions on neural systems and rehabilitation engineering: a publication of the IEEE Engineering in Medicine and Biology Society. 2006; 14:246–50.
25. Brunner P, Ritaccio AL, Emrich JF, Bischof H, Schalk G. Rapid Communication with a “P300” Matrix Speller Using Electrocorticographic Signals (ECoG). Frontiers in neuroscience. 2011; 5:5. [PubMed: 21369351]
26. Streetman, BG.; Banerjee, SK. Solid State Electronic Devices. Pearson: 1981.
27. Viventi J, et al. A Conformal, Bio-Interfaced Class of Silicon Electronics for Mapping Cardiac Electrophysiology. Science Translational Medicine. 2010; 2:24ra22–24ra22.
28. Yanagisawa T, et al. Neural decoding using gyral and intrasulcal electrocorticograms. Neuro Image. 2009; 45:1099–106. [PubMed: 19349227]
29. Besson P, Andermann F, Dubeau F, Bernasconi A. Small focal cortical dysplasia lesions are located at the bottom of a deep sulcus. Brain. 2008; 131:3246–55. [PubMed: 18812443]
30. Stieglitz T. Flexible biomedical microdevices with double-sided electrode arrangements for neural applications. Sensors and Actuators A: Physical. 2001; 90:203–211.
31. Stieglitz T. Flexible BIOMEMS with electrode arrangements on front and back side as key component in neural prostheses and biohybrid systems. Sensors and Actuators B: Chemical. 2002; 83:8–14.
32. Thompson SE, et al. A 90-nm Logic Technology Featuring Strained-Silicon. IEEE Transactions on Electron Devices. 2004; 51:1790–1797.
33. Kim D-H, et al. Dissolvable films of silk fibroin for ultrathin conformal bio-integrated electronics. Nature materials. 2010:1–8.10.1038/nmat2745 [PubMed: 20019657]
34. Padnick LB, Linsenmeier R. a Properties of the flash visual evoked potential recorded in the cat primary visual cortex. Vision research. 1999; 39:2833–40. [PubMed: 10492813]
35. Tusa RJ, Rosenquist AC, Palmer L. a Retinotopic organization of areas 18 and 19 in the cat. The Journal of comparative neurology. 1979; 185:657–78. [PubMed: 447876]
36. Hinton GE, Salakhutdinov RR. Reducing the dimensionality of data with neural networks. Science (New York, NY). 2006; 313:504–7.
37. Larochelle, H.; Erhan, D.; Courville, A.; Bergstra, J.; Bengio, Y. An empirical evaluation of deep architectures on problems with many factors of variation. Proceedings of the 24th international conference on Machine learning - ICML ’07; 2007. p. 473-480.
38. Anderson WS, Kudela P, Cho J, Bergey GK, Franaszczuk PJ. Studies of stimulus parameters for seizure disruption using neural network simulations. Biological cybernetics. 2007; 97:173–94. [PubMed: 17619199]
39. Witkowski FX, et al. Spatiotemporal evolution of ventricular fibrillation. Nature. 1998; 392:78–82. [PubMed: 9510250]
40. Prechtl JC, Cohen LB, Pesaran B, Mitra PP, Kleinfeld D. Visual stimuli induce waves of electrical activity in turtle cortex. Proceedings of the National Academy of Sciences of the United States of America. 1997; 94:7621–6. [PubMed: 9207142]
41. Huang X, et al. Spiral waves in disinhibited mammalian neocortex. The Journal of neuroscience: the official journal of the Society for Neuroscience. 2004; 24:9897–902. [PubMed: 15525774]

42. Huang X, et al. Spiral Wave Dynamics in Neocortex. Neuron. 2010; 68:978–990. [PubMed: 21145009]
43. Hastie, T.; Tibshirani, R.; Friedman, J. The Elements of Statistical Learning. Springer-Verlag; New York, New York, USA: 2001.
44. Tibshirani R, Walther G, Hastie T. Estimating the number of clusters in a data set via the gap statistic. Journal of the Royal Statistical Society: Series B (Statistical Methodology). 2001; 63:411–423.
45. Blanco JA, et al. Unsupervised classification of high-frequency oscillations in human neocortical epilepsy and control patients. Journal of neurophysiology. 2010; 104:2900–12. [PubMed: 20810694]
46. Paullet JE, Ermentrout GB. Stable Rotating Waves in Two-Dimensional Discrete Active Media. SIAM Journal on Applied Mathematics. 1994; 54:1720.
47. Gais S, Mölle M, Helms K, Born J. Learning-dependent increases in sleep spindle density. The Journal of Neuroscience. 2002; 22:6830–4. [PubMed: 12151563]
48. Tamminen J, Payne JD, Stickgold R, Wamsley EJ, Gaskell MG. Sleep Spindle Activity is Associated with the Integration of New Memories and Existing Knowledge. Journal of Neuroscience. 2010; 30:14356–14360. [PubMed: 20980591]
49. Sekitani T, et al. A large-area wireless power-transmission sheet using printed organic transistors and plastic MEMS switches. Nature materials. 2007; 6:413–7. [PubMed: 17468763]
50. Llinás RR, Ribary U, Jeanmonod D, Kronberg E, Mitra PP. Thalamocortical dysrhythmia: A neurological and neuropsychiatric syndrome characterized by magnetoencephalography. Proceedings of the National Academy of Sciences of the United States of America. 1999; 96:15222–7. [PubMed: 10611366]
51. Cardin JA, Palmer LA, Contreras D. Stimulus feature selectivity in excitatory and inhibitory neurons in primary visual cortex. Journal of Neuroscience. 2007; 27:10333. [PubMed: 17898205]
52. Cardin JA, Palmer LA, Contreras D. Cellular mechanisms underlying stimulus-dependent gain modulation in primary visual cortex neurons in vivo. Neuron. 2008; 59:150–60. [PubMed: 18614036]
53. Taylor Z, Miller K. Reassessment of brain elasticity for analysis of biomechanisms of hydrocephalus. Journal of biomechanics. 2004; 37:1263–9. [PubMed: 15212932]

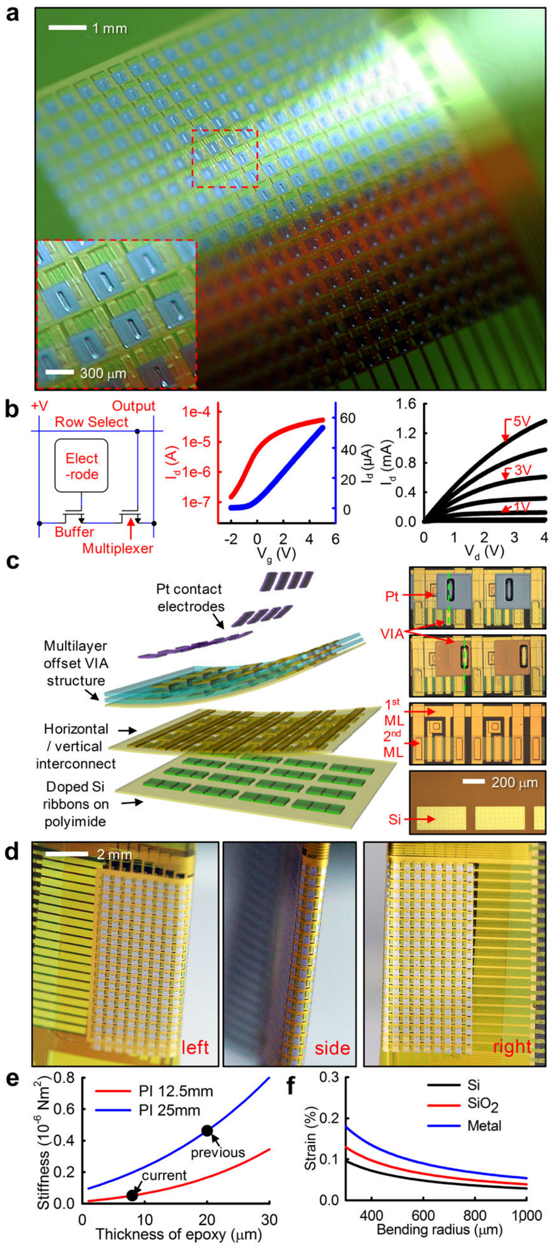

Figure 1. Flexible, high-resolution multiplexed electrode array

a, Photograph of a 360 channel high density active electrode array. The electrode size and spacing was 300 μm × 300 μm and 500 μm, respectively. (inset) A closer view showing a few unit-cells. **b,** Schematic circuit diagram of single unit-cell containing two matched transistors (left), transfer characteristics of drain-to-source current (I_{ds}) from a representative flexible transistor on linear (blue) and logarithmic (red) scales as gate to source voltage (V_{gs}) was swept from −2 to +5 V, demonstrating the threshold voltage (V_t) of the transistor (center). Current-voltage characteristics of a representative flexible silicon transistor (right). I_{ds} was plotted as a function of drain-to-source voltage (V_{ds}). V_{gs} was varied from 0 to 5 V in 1–V steps. **c,** Schematic exploded view (left) and corresponding microscope image of each layer: doped silicon nanoribbons (right frame, bottom), after vertical and horizontal interconnection with arrows indicating the 1st and 2nd metal layers (ML) (right frame, 2nd from bottom), after water-proof encapsulation (right frame, 3rd from bottom) and after platinum electrode deposition (right frame, top). Green dashed lines illustrated the offset via structure, critical to preventing leakage current while submerged in conductive fluid. **d,** Images of folded electrode array around low modulus Polydimethylsiloxane (PDMS) insert. **e,** bending stiffness of electrode array for varying epoxy thicknesses and two different PI substrate thicknesses. A nearly 10-fold increase in flexibility between the current device and our prior work was shown. **f,** Induced strain in different layers depending on the change in bending radius.

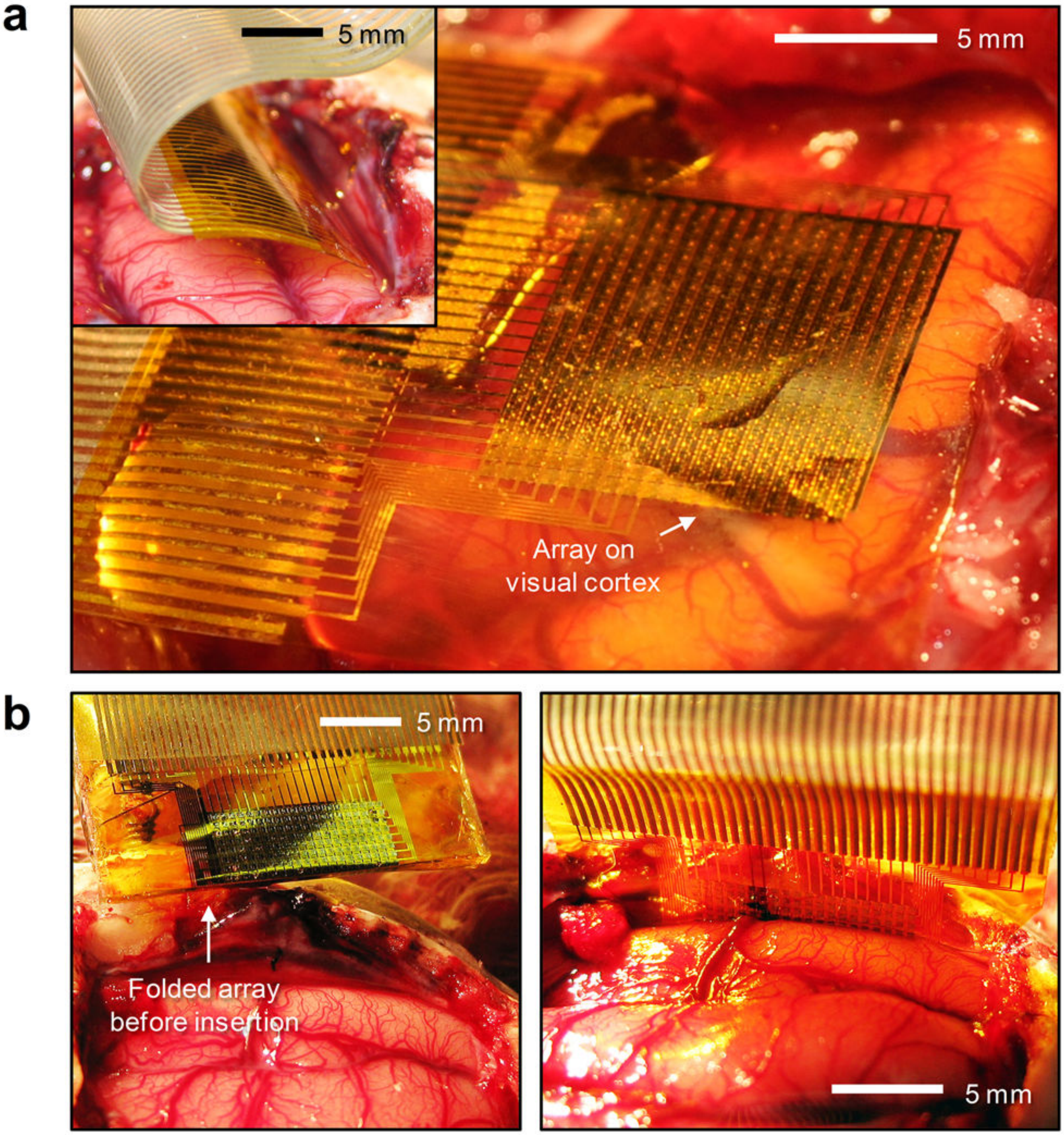

Figure 2. Animal experiment using feline model

a, A flexible, high-density, active electrode array placed on the visual cortex. (inset) The same electrode array inserted into the interhemispheric fissure. **b,** Folded electrode array before insertion into the interhemispheric fissue (left). Flat electrode array inserted into the interhemispheric fissure (right).

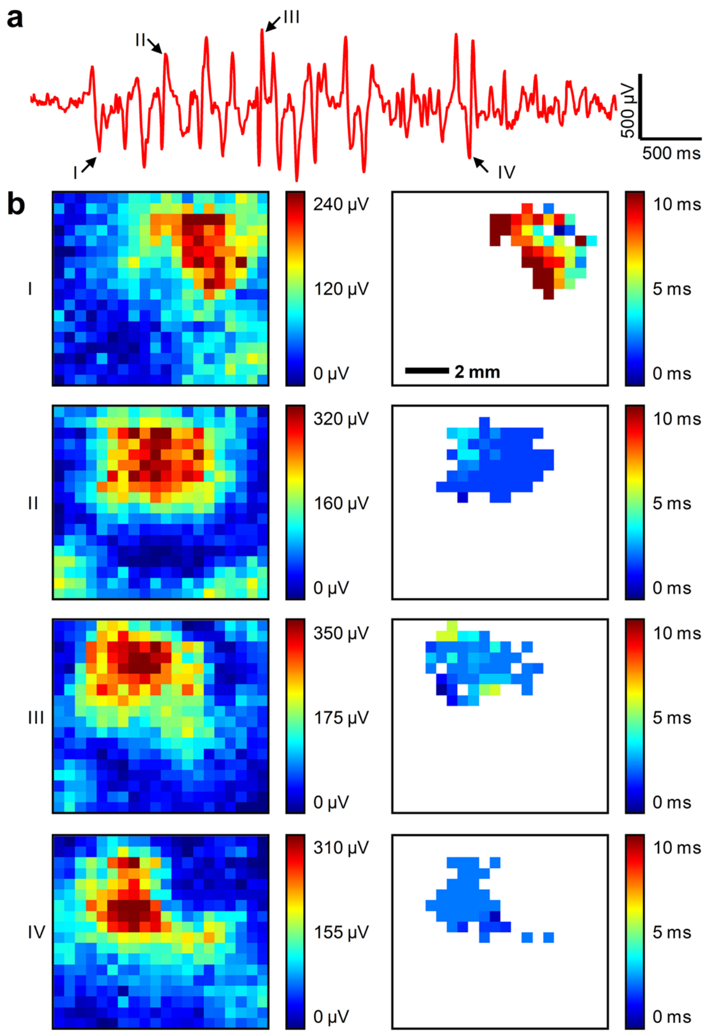

Figure 3. Spontaneous barbiturate-induced sleep spindles

a, A typical spindle recorded from a representative channel. Negative is plotted up by convention. Arrows point to individual spikes of the spindle (I – IV) further analyzed in the following panel. **b,** Root-mean-square (RMS) value of the zero-meaned signal of individual sharply contoured waves comprising the spindle demonstrated the high sensitivity of the electrode array and the spatially-localized nature of spindles (left column) as well as the high degree of temporal synchronization indicated by the relative time to peak across the array (right column). Data are anatomically orientated as shown in the inset of Figure 4b.

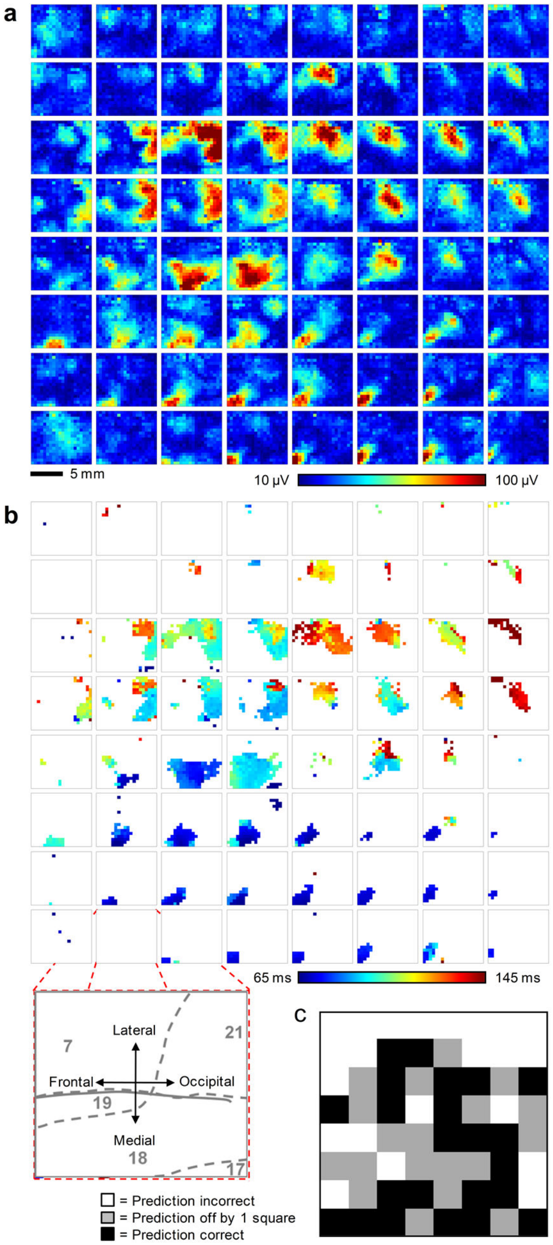

Figure 4. Visual evoked response analysis to a 2-dimensional sparse noise visual stimulus

a, 64 color maps, each showing the response (root-mean-square (RMS) value of the zero-meaned signal within the response window) of the entire 360 channel electrode array. The color maps are arranged in the same physical layout as the stimuli are presented on the monitor, i.e. the image map in the upper left hand corner of the figure represents the neural response across the entire array to a flashing box presented in the upper left hand corner of the monitor. The color scale is constant over all 64 image maps and is saturated at the 1st and 99th percentile respectively to improve the visual display. **b,** 64 color maps generated from the same response data as in a, but plotting the response latency in ms. Channels that did not show a strong response, as determined by exceeding 50% of the maximum evoked response, were excluded and are colored white. (inset) Exploded view illustrates the anatomical orientation of the electrode array on the brain and approximate location of Brodmann's areas (grey numbers and dashed lines). **c,** Performance results achieved after subjecting a test set of data to a deep belief net classifier in accurately determining each originating location on the screen of respective stimuli. 23 of the 64 screen locations (36%) were predicted exactly correct (black boxes), significantly better than chance (1.6%). 42 of 64 (66%) screen locations were predicted correctly within one neighboring square (grey boxes, distance ≤ √2, chance level 11.8%).

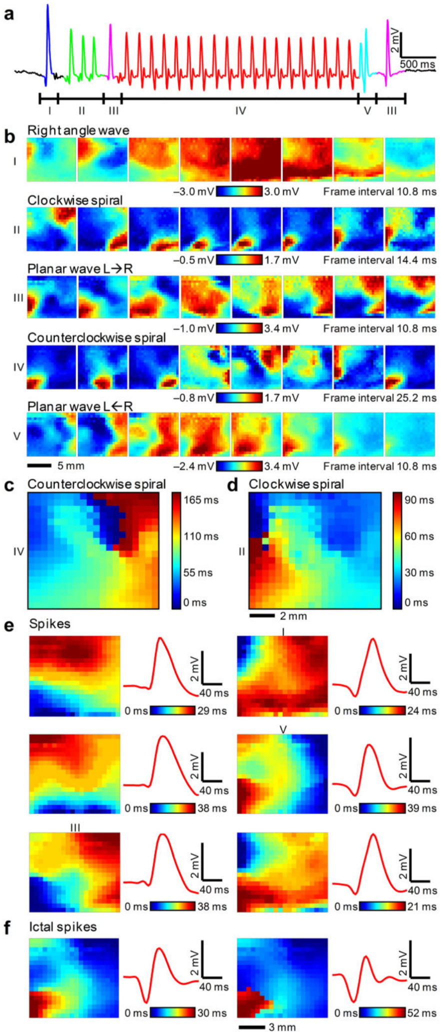

Figure 5. Detailed 2-dimensional data from electrographic seizures in feline neocortex

a, μECoG signal from a representative channel of the electrode array during a short electrographic seizure. Negative is plotted up by convention. Labelled segments correspond to movie frames below. **b**, Movie frames show varied spatial-temporal μECoG voltage patterns from all 360 electrodes during the labelled time intervals from Figure 5a. The frame interval and color scale are provided for each set of 8 movie frames and the color scale is saturated at the 2nd and 98th percentile respectively over 8 frames to improve the visual display. Data are anatomically orientated as shown in the inset of Figure 4b. c, Relative delay map for the 4 to 8 Hz band-pass filtered data from 3 seconds of continuous clockwise spiral rotations (Fig. 5b, waveform IV) illustrating a clear phase singularity and counter clockwise rotation. **d,** Relative delay map for narrow band-pass filtered data from ~0.5 seconds of clockwise spiral rotations (Fig. 5b, waveform II) illustrating clockwise rotation, but a less clear singularity. **e,** Representative delay image maps from six different spike clusters are shown to illustrate the differences between clusters (left columns). The average waveform for the corresponding spike (red traces, right columns) illustrates that complicated spatial patterns at the micro scale (0.5 mm) can be indistinguishable at the current clinical scale (~10mm). Numerals I, III and V indicate the clusters that the corresponding waves in Fig. 5b belong to. **f,** Representative delay image maps from two clusters that occurred almost exclusively during seizures, illustrating striking differences in spatial-temporal micro scale patterns during seizures.